



1 **Technical note: Rapid phase identification of apatite and zircon grains for geochronology**
2 **using X-ray micro-computed tomography**

3 Emily H. G. Cooperdock^{1*}, Florian Hofmann^{1,2*}, Ryley M. Collins¹, Anahi Carrera¹, Aya
4 Takase³, and Aaron J. Celestian⁴

5 ¹University of Southern California, Department of Earth Sciences, 3651 Trousdale Parkway, Los
6 Angeles, CA 90089, USA

7 ²University of Alaska Fairbanks, Geophysical Institute, 900 Yukon Dr, Fairbanks, AK 99775,
8 USA

9 ³Rigaku Americas Corporation, 9009 New Trails Drive, The Woodlands, TX 77381, USA

10 ⁴Mineral Sciences Department, Natural History Museum of Los Angeles County, 900 Exposition
11 Boulevard, Los Angeles, California 90007, USA

12 *Authors contributed equally to this work.

13 *Correspondence to:* cooperdo@usc.edu



14 **Abstract**

15 Apatite and zircon are among the best-studied and most widely used accessory minerals
16 for geochronology and thermochronology. Given that apatite and zircon are often present in the
17 same lithologies, distinguishing the two phases in crushed mineral separates is a common
18 challenge that many laboratories face. Here we present a method for efficient and accurate
19 apatite and zircon mineral phase identification using X-ray micro-computed tomography
20 (microCT) of grain mounts that provides additional 3-dimensional grain size, shape, and
21 inclusion suite information. In this study, we analyzed apatite and zircon grains from Fish
22 Canyon Tuff samples that underwent methylene iodide (MEI) and lithium heteropolytungstate
23 (LST) heavy liquids density separations. We validate the microCT results using known standards
24 and phase identification with Raman spectroscopy demonstrating that apatite and zircon are
25 distinguishable from each other and other common phases, e.g., titanite, based on microCT X-ray
26 density. We present recommended microCT scanning protocols after systematically testing the
27 effects of different scanning parameters and sample positions. This methodology can help to
28 reduce time spent performing density separations with highly toxic chemicals and visually
29 inspecting grains under a light microscope, and the improved mineral identification and
30 characterization can make geochronologic data more robust.

31

32 **1 Introduction**

33 Apatite and zircon are mineral phases widely used for geochronology and
34 thermochronology using the U-Pb (e.g., Bowring and Schmitz, 2003), (U-Th)/He (e.g. Farley,
35 2002), and fission track (e.g. Tagami and O’Sullivan, 2005) methods. Correct identification of
36 these phases (e.g. Guenther et al., 2016), characterization of the crystal shape (Farley et al.,
37 1996), and the absence of mineral and fluid inclusions (e.g. Lippolt et al., 1994; Vermeesch et
38 al., 2007) are important factors in producing reliable, high-quality geochronologic data. The
39 standard approach to selecting apatite and zircon grains for geochronology is to 1) crush and
40 grind rock samples into their mineral constituents, 2) perform magnetic and density separation
41 using a Frantz isodynamic separator and heavy liquids to filter for the mineral of choice, and
42 then 3) pick individual grains from these separates under a transmitted light microscope
43 (Gautheron et al., 2021).



44 Different heavy liquid solutions used for density separation can either produce grain
45 fractions that have apatite and zircon mixed together or separated (e.g., Dumitru and Stockli,
46 1998; Koroznikova et al., 2008). The density of apatite ($\text{Ca}_5(\text{PO}_4)_3(\text{F},\text{OH},\text{Cl})$) is 3.10-3.25 g/cm^3
47 and depends on the solid solution composition between fluorapatite, chlorapatite, and
48 hydroxylapatite (Hughes et al., 1989). Zircon (ZrSiO_4) can display densities between 3.9 and 4.7
49 g/cm^3 , depending on the degree of metamictization (Holland and Gottfried, 1955). Although
50 density-separated apatite and zircon fractions make picking the correct mineral easier (Dumitru
51 and Stockli, 1998), the process often includes the use of toxic halogenated organic solutions,
52 such as bromoform (CHBr_3) and diiodomethane (CH_2I_2 , methylene iodide, commonly
53 abbreviated as MEI, MI, or DIM; e.g. Hauff and Airey, 1980). Typically, bromoform (2.89
54 g/cm^3) is used in a first step to separate quartz and feldspar and the resulting heavy fraction is
55 then treated with MEI (3.32 g/cm^3) to separate apatite and zircon (e.g. Dumitru and Stockli,
56 1998).

57 Both Bromoform and MEI are known to be toxic. Specifically, MEI can cause acute
58 symptoms through skin contact or inhalation, and acute toxicity and death have been documented
59 for a case of ingestion (Weimerskirch et al., 1990). MEI has also been shown to be mutagenic
60 meaning acute or long-term exposure may impact reproductive health, particularly in pregnant
61 women (Van Bladeren et al., 1980; Osterman-Golkar et al., 1983; Buijs et al., 1984; Roldán-
62 Arjona and Pueyo, 1993). In addition, samples separated with MEI are typically washed with
63 acetone, and the mixture of these chemicals is highly flammable. Burning MEI has the potential
64 to produce large amounts of free iodine, which also poses a significant health risk (Hauff and
65 Airey, 1980). Due to its toxicity, MEI must be used in a vent hood with proper personal
66 protective equipment (PPE) and requires special training in safe handling techniques (Dumitru
67 and Stockli, 1998).

68 Safety precautions required for hazardous chemical handling may exclude workers or
69 students with conditions that do not allow them to comply with the safety precautions. For
70 example, personal protective equipment may only be available in restricted sizes, and fume hood
71 design is often incompatible with the use of wheelchairs or other mobility devices. Thus,
72 eliminating hazardous chemicals from laboratory procedures results in both a safer work
73 environment and a more inclusive workplace.



74 Many labs elect to use lithium heteropolytungstate (LST), lithium metatungstate (LMT),
75 and sodium polytungstate (SPT) because they are generally non-toxic and relatively inert
76 (Munsterman and Kerstholt, 1996; Mountenay, 2011). Similar to bromoform (but less toxic)
77 these heavy liquids can be used at densities of 2.8-3.0 g/cm³ to remove quartz and feldspar from
78 the separate, but they do not separate apatite from zircon. Zircon and apatite crystals in natural
79 samples exhibit a wide variety of morphologies depending on the sample history and can be
80 difficult to distinguish by eye under a binocular microscope despite the fact that they have
81 different compositions and crystal structures. Optical methods such as crossed polarizers are
82 often used in addition to crystal shape to distinguish these phases from each other as well as from
83 other phases such as titanite, xenotime, monazite, allanite, rutile, baddeleyite, etc., but are not
84 always able to uniquely identify the phase of a particular grain.

85 Mistaken mineral identification can lead to significant issues in data analysis, quality, and
86 interpretation. Depending on the geochronologic technique employed, this misidentification
87 might be detected further along in the analytical procedures. In (U-Th)/He analysis, a mistake
88 may be realized during degassing or dissolution. Due to their differential diffusion behavior,
89 zircon usually requires higher temperatures and longer laser-heating times to fully extract He
90 than for apatite (e.g. Farley, 2002). Apatite dissolves readily in a weak nitric acid, whereas zircon
91 needs to be subjected to extensive Parr bomb pressure dissolution procedures using a mixture of
92 nitric acid, hydrochloric acid, and hydrofluoric acid to be completely dissolved (Farley, 2002).
93 As a result, a misidentified mineral may not be completely degassed or dissolved during the
94 analytical procedure, leading to erroneous results. The presence of Ca or Zr in dissolved mineral
95 solutions can be used during subsequent isotope-dilution ICP-MS analysis to test whether the
96 correct phase was chosen for the analysis, as was demonstrated for (U-Th)/He by Guenther et
97 al. (2016).

98 Similar issues arise in other methods. In laser ablation analysis as part of U-Pb or (U-
99 Th)/He dating, the ablation characteristics and the presence of Ca or Zr in the analyte can be used
100 as diagnostic criteria. Etching parameters for fission track, such as the type and molarity of acids,
101 etching time, and temperature conditions, are highly phase-specific and need to be tightly
102 controlled to yield reproducible and internally consistent data (Tagami and O'Sullivan, 2005).
103 Applying zircon etching procedures to apatite grains might lead to the complete loss of a sample.



104 Given the amount of time and materials required by these analytical methods,
105 misidentification of minerals can lead to significant monetary and time-effort losses. Therefore,
106 an efficient pre-screening technique to confirm apatite and zircon phases for geochronologic and
107 thermochronologic application can help to avoid unsuccessful partial analyses of misidentified
108 samples and lead to more robust and reproducible data. Many laboratories have developed
109 techniques to reduce mineral misidentification. These can include having a more experienced
110 user look over selected grains, analyzing pre-selected grains under a scanning electron
111 microscope (SEM) to measure elemental compositions with energy dispersive spectroscopy
112 (EDS), using Raman spectroscopy for phase identification, and others.

113 We test whether X-Ray micro-computed tomography (microCT) scanning can be used as
114 an effective pre-screening tool to distinguish between apatite and zircon and to detect
115 misidentification of grains. The difference in apatite and zircon composition and densities (3.1-
116 3.2 g/cm³ and 3.9-4.7 g/cm³, respectively) lead to differential X-ray absorption, which yields
117 characteristic grayscale value contrast in microCT data (e.g. Ketcham and Carlson, 2001). In
118 addition to phase identification, microCT data yields high-resolution 3-dimensional grain shape
119 measurements and reveals internal heterogeneities, such as fractures or inclusions (Evans et al.,
120 2008; Glotzbach et al., 2019; Cooperdock et al., 2019). Resolution varies by instrument and
121 acquisition parameters; the instrument used in this study achieves a maximum voxel resolution
122 of ~2 μm/10 μm³. We explore different acquisition parameters to optimize the distinction
123 between different minerals and minimize the scan time to yield a streamlined procedure for
124 routine pre-screening of mineral grains for geochronologic applications.

125 **2 Materials and methods**

126 **2.1 Mineral separation**

127 We selected Fish Canyon Tuff (FCT) as a test sample because it contains both apatite and
128 zircon and is used as an age standard in many applications of geo- and thermochronology
129 (McDowell et al., 2005; Donelick et al., 2005). We obtained three separate FCT samples: one
130 mineral separate of a MEI heavy fraction given to us by the UTChron Laboratory at the
131 University of Texas at Austin (UT-FCT), and two that we collected from two FCT localities near
132 Monte Vista, CO (USC-FCT1: 37°36'38.73" N, 106°42'19.93" W; USC-FCT2: 37°38'22.21" N,



133 106°17'57.77" W). The two whole-rock samples were crushed on a jaw crusher and disk mill at
134 the University of Southern California. Crushed samples were sieved and the 75-250 μm size
135 fraction was washed before using a hand magnet and a Frantz isodynamic magnetic separator to
136 remove magnetic fractions. Samples then underwent density separation using lithium
137 heteropolytungstate (LST). This is a water-based, low-toxicity heavy liquid with a maximum
138 density of 2.85 g/cm^3 at room temperature that produces a heavy mineral separate with apatite
139 and zircon (and other phases) mixed together. Sample types and names are summarized in Table
140 1.

141 The UT-FCT separate supplied by the University of Texas at Austin was processed using
142 the same mineral separations procedures with the following exceptions: the samples were density
143 separated on a Gemeni water table prior to magnetic separation, and the sample experienced a
144 two-step heavy liquids separation using bromoform and MEI. These heavy liquids are more toxic
145 than LST but have densities of 2.95 g/cm^3 and 3.32 g/cm^3 , respectively, and should yield grain
146 fractions that separate apatite from zircon. Only the MEI heavy fraction was used for this
147 experiment.

148 As a reference for microCT imaging, we used mineral standards for apatite, zircon, and
149 titanite from existing collections. Two Durango apatite standards from large apatite crystals were
150 supplied by the UTChron laboratory at the University of Texas at Austin (UT-DUR) and Caltech
151 (CIT-DUR). We used shards from large crystals of Sri Lankan zircon (SL1) from Caltech (Farley
152 et al., 2020) and Minas Gerais titanite (MG1) from the Natural History Museum of Los Angeles
153 County (more specific sample location information is not known). These standard crystals were
154 gently hand crushed and sieved to $<75 \mu\text{m}$, $75\text{-}250 \mu\text{m}$, and $>250 \mu\text{m}$ size fractions.

155

156 Table 1. Mineral standards and unknowns used in this study. Large standard crystals were
157 crushed to obtain shards to be used as a reference for microCT analyses. Unknown grains were
158 extracted from FCT whole-rock samples.

Sample	Minerals	Type	Grain type	Sample Name	Density Separation
UT-DUR	Apatite	Standard	Shard	Durango	none
CIT-DUR	Apatite	Standard	Shard	Durango	none
SL1	Zircon	Standard	Shard	Sri Lanka	none



Sample	Minerals	Type	Grain type	Sample Name	Density Separation
MG1	Titanite	Standard	Shard	Minas Gerais	none
UT-FCT	Apatite, Zircon	Unknown	Grain	Fish Canyon Tuff	bromoform, MEI
USC-FCT1	Apatite, Zircon, Titanite	Unknown	Grain	Fish Canyon Tuff	LST
USC-FCT2	Apatite, Zircon, Titanite	Unknown	Grain	Fish Canyon Tuff	LST

159

160 2.2 Making crystal mounts

161 Graduate students were tasked with picking mineral grains that looked like apatite or
162 zircon and covered a range of grain sizes and morphologies from the three FCT samples using a
163 Nikon SMZ25 optical microscope. It is notable that all samples, including the MEI separate,
164 yielded both apatite and zircon. The selected grains were placed onto grain mounts for microCT
165 analysis (see Sect. 2.3). Each mount also included known mineral standards for reference and
166 normalization (Fig. 1a). Three grain mounts were constructed (Mount A, B, and C, see Fig. 2).
167 Mount A included 36 grains from UT-FCT “unknowns,” 10 shards of SL1 zircon, and 15 shards
168 of CIT-DUR apatite. Mount B included 39 grains of USC-FCT1 “unknowns,” 32 grains of USC-
169 FCT2 “unknowns,” 9 shards of SL1 zircon, and 24 shards of UT-DUR apatite. Mount C included
170 11 shards of SL1 zircon, 15 shards of CIT-DUR apatite, and 15 shards of MG1 titanite standards.
171 We used the 75-250 μm size fraction and $>250 \mu\text{m}$ size fractions of the mineral standards to test
172 the impact of grain size on grayscale values in microCT data. On Mount C, individual shards
173 from each mineral were distributed evenly across the mount to test whether there is any spatial
174 variability in X-ray attenuation and grayscale.

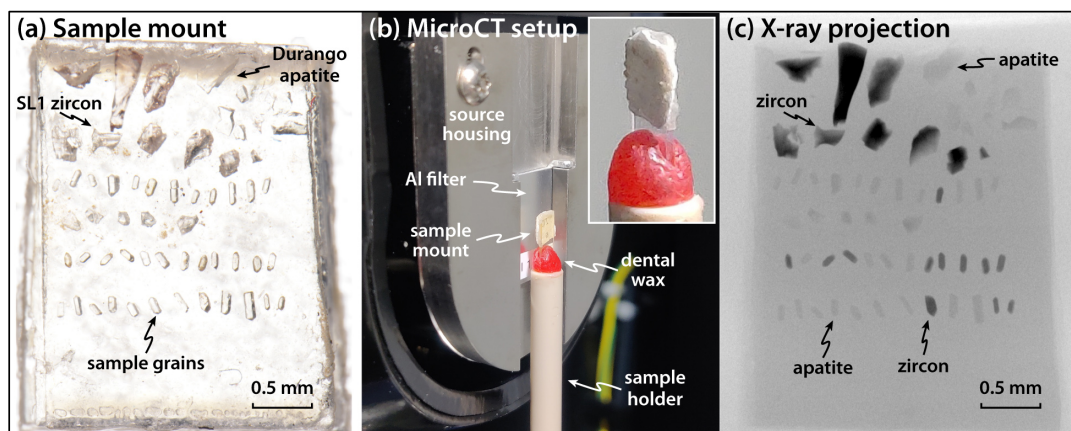
175 We assembled grain mounts by cutting small plastic shapes (rectangles, squares, or
176 circles) out of 1 mm thick plastic slides and placing double-sided adhesive tape on one side.
177 Mounts for vertical scans (when the mount is standing upright on the top of the sample holder)
178 were constructed by cutting ~ 3 mm by 4 mm rectangles from plastic slides of 1 mm thickness,
179 which was covered with double-sided adhesive tape. Grains were placed on the upper part of the
180 rectangle mount (Fig. 1a), and the end without grains was inserted into dental wax to hold the



181 mount in place, vertically, on top of the sample holder (Fig. 1b). We tested different brands of
182 double-sided adhesive tape and found that some brands appear clear under a transmitted light
183 microscope while others have significant interference colors and visible fibers. Double-sided
184 tape selection did not affect microCT data.

185 Prior to placing the grains, the plastic mounts were temporarily secured to a glass slide
186 with double-sided tape to hold them in place. Individual crystals were selected from mineral
187 separates and placed on the tape using tweezers and needles under a light microscope. Grains
188 were spaced to avoid touching, with up to 104 total crystals per mount. Optical micrographs of
189 the mount and each individual crystal were taken with transmitted and reflected light as well as
190 with crossed polarizers.

191



192

193 Figure 1: (a) Transmitted light micrograph of a sample mount with known apatite and zircon
194 standard shards and unknown sample grains made from a plastic slide and double-sided tape,
195 about 3 mm in width. (b) Sample mount installed vertically in the microCT instrument secured
196 on top of a sample holder with dental wax. Insert shows a closer view of the sample mount in
197 measurement position. (c) X-ray projection of the same mount as in (a). Zircon grains show up as
198 darker (more X-ray absorption) than apatite grains. The brightness in projections is controlled by
199 the material-specific X-ray attenuation as well as by the integrated thickness of the traversed
200 material.



201 2.3 MicroCT scanning

202 All microCT scans were acquired on a Rigaku CT Lab HX130 benchtop microCT
203 instrument at the USChelium Laboratory at the University of Southern California. Individual
204 mounts were installed vertically (perpendicular to the X-ray beam direction, parallel to the
205 detector plane; see Fig. 1b) in order to minimize the effect of interference from X-ray artifacts
206 such as shadowing between individual grains due to beam hardening and photon starvation (see
207 Section 3.2 and Fig. 7). Mounts were scanned at accelerating voltages of 130 and 60 kV with
208 currents of 61 and 133 μA , respectively. We used a 1.0 mm thick aluminum filter to selectively
209 remove lower energies from the polychromatic beam in order to reduce the effect of beam
210 hardening (see Hanna and Ketcham, 2017, for details). Total instrument run times were between
211 18 seconds and 125 minutes using continuous and step scanning with a field of view (FOV) of 5
212 mm diameter and 3.8 mm height (see Table 2). Continuous scans were done for 18 s, 4 min, 17
213 min, and 68 min. Over this time, the sample is rotated and X-rays are continuously counted on
214 the detector. We also performed 125 minute step scans (500 ms exposure time, 1500 projections,
215 4 integrations), in which the sample is rotated in steps and the detector moves between the steps
216 to reduce ring artifacts. As a result, the 125 minute scan time includes 50 minutes of actual X-ray
217 exposure and 75 minutes of instrument adjustment. Note, in continuous scans the scan time and
218 exposure time are the same because there is no detector adjustment. We report the total
219 instrument scan time in Table 2 and the total exposure time on Figure 7. Reconstructions were
220 computed using the Rigaku CT Reconstruction software. Continuous scans were reconstructed to
221 yield volumes with a width and length of 1024 voxels. Step scans were integrated for longer
222 times than the continuous scans and yielded enough data to be processed at full resolution
223 (width/length of 2784 voxels) while maintaining a usable signal-to-noise ratio.

224

225 Table 2. Scan parameters tested in this study.

Scan voltage (kV)	Scan type	Total scan times (minutes)	Voxel size (μm)	Volume size (pixels)	File size (GB)
60 and 130	continuous	0.3, 4, 17, 68	5.7	1024x1024x708	1.4 (0.2 cropped)
60 and 130	step	125	2.1	2784x2784x1931	27.8 (2.4 cropped)



226 **2.4 MicroCT data analysis**

227 The reconstructed microCT data was processed with Dragonfly (Version 2021.1) by
228 Object Research Systems. Reconstructed volumes of each mount with all different scan times
229 and X-ray energies were loaded into Dragonfly. The volumes scanned at 60 kV for 68 min were
230 used as a reference since they displayed the best signal-to-noise ratio of all the tested scan
231 parameters. Volumes were registered relative to the 60 kV/68 min scans using the Image
232 Registration tool, which translates and rotates volumes to align scans. Grains were segmented in
233 the 60 kV/68 min scan volumes by creating regions of interest (ROI) using histographic
234 segmentation, which delineates grains from their surroundings (air or adhesive tape) based on
235 threshold grayscale values. The resulting volumes were filtered by applying a 3D opening
236 operation (a combination of erosion and dilation which removes small objects, like dust, while
237 not changing the geometry of large volumes) and eroded by one voxel to remove the effect of
238 rapid changes in grayscale value near the grain boundary.

239 Each grain was separated into an ‘object’ by creating a Multi-ROI (a ROI that contains
240 multiple objects) from continuous segments in which voxels are connected by at least one of
241 their faces (6-connected). Each grain ‘object’ consists of hundreds to thousands of voxels that
242 can be used to calculate grayscale statistics. Small fragments separated from larger grains of less
243 than 100 voxels were not used for further analysis to ensure the measurements have statistical
244 significance. In this way, individual grains were mapped out and distinguished from other small
245 objects in the scan (e.g., chipped pieces or detritus on the adhesive tape). The geometry of the
246 segmented objects was resampled to fit each volume, and information on the position, size,
247 surface area, and greyscale value distribution of each grain was extracted from the Multi-ROIs.

248 Absolute grayscale values can change between scans since they are dependent on the
249 scan geometry, acquisition parameters, arrangement of grains, and processing, with internal
250 normalization and scaling being applied during reconstruction. To make scans comparable, we
251 chose to normalize the grayscale values of all grains on a mount by the average grayscale value
252 of the SL1 zircon grains in the same volume. We also computed the ratio of the grayscale values
253 of the 60 kV and 130 kV scans with otherwise identical scan parameters to yield a dual-energy
254 parameter.



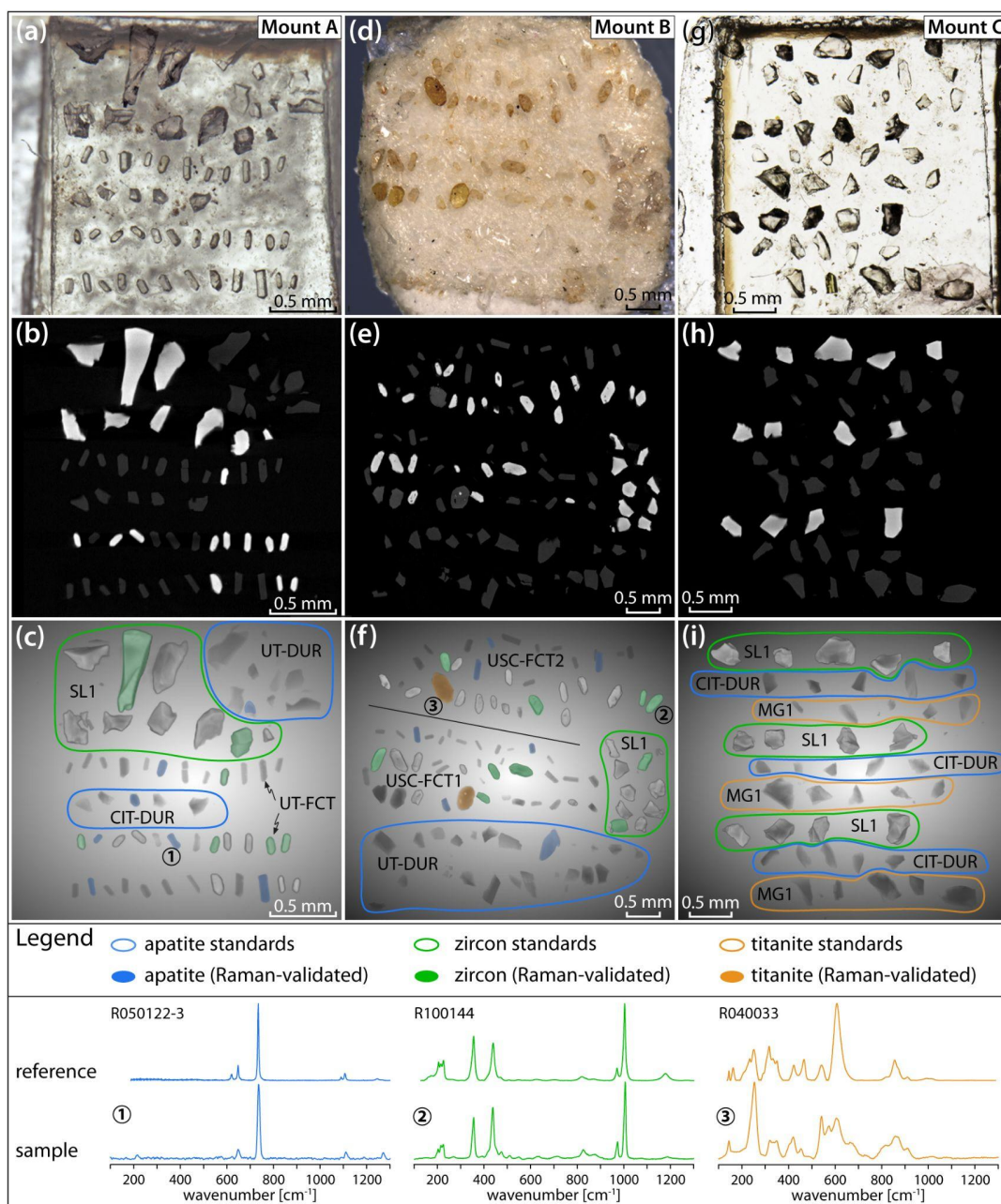
255 **2.5 Phase validation by Raman spectroscopy**

256 To validate the different phases observed in microCT data, we determined the mineral
257 phase of 35 grains in Mounts A and B by Raman spectroscopy. This included a subset of 28
258 unknown grains from FCT samples and 7 shards of known mineral standards (Fig. 2).
259 Representative grains were selected to encompass a range of grain sizes and morphologies,
260 positions on the mount, and microCT grayscale contrast. After microCT scanning, the grain
261 mounts were transferred to a glass slide, and grains were analyzed using a HORIBA XploRA
262 PLUS spectrometer at the Natural History Museum of Los Angeles County. Apatite, zircon, and
263 titanite were identified by matching baseline-corrected spectra with comparison spectra from the
264 RRUFF database (Lafuente et al., 2005) using CrystalSleuth. Raman spectral analyses were
265 conducted using a green 532 nm diode laser at 50% laser power, a diffraction grating of 1880
266 gr/mm, a 100x (0.9 NA) objective, 200 μm slit, and 300 μm pinhole for confocal optical
267 geometry. Raman spectra were collected in the range of 100-1600 cm^{-1} with each grain analyzed
268 with a 3 s exposure averaged from 10 acquisitions.

269

270

271



272

273 Figure 2: Transmitted light micrographs (a,d,g), microCT slices (b,e,h), and microCT volume
 274 renderings (c,f,i) of Mounts A, B, and C. MicroCT slices show a large contrast between
 275 apatite/titanite (darker) and zircon grains (brighter). Grayscale color and grain relief in 3D
 276 renderings are distinct for different mineral phases. The 3D renderings show Raman-validated



277 grains highlighted and known standard shards circled in blue (apatite), green (zircon), and
278 titanite (orange). Baseline-corrected Raman spectra of representative grains and reference spectra
279 from the RRUFF database (including record numbers) are shown below the images. Numbers in
280 circles indicate the grains in the volume renderings which correspond to the sample Raman
281 spectra.

282 **3 Results and discussion**

283 Different microCT scanning parameters were systematically tested on the same three
284 grain mounts to determine the optimal scan conditions for distinguishing between mineral phases
285 while minimizing cost, time, and data file sizes. Individual microCT data file sizes range from 2
286 to 28 GB depending on acquisition and processing parameters. Reconstructing and manipulating
287 large datasets can require specialized computers with demanding system requirements for data
288 storage, memory, and processing power. The microCT data for single grain mounts, like the ones
289 used in this study, can be cropped to produce manageable file sizes that can be viewed and
290 analyzed without the need for specialized computers. We determined that for the instrument used
291 here a continuous scan time of 17 min at 60 kV (5.7 μm resolution) is sufficient for mineral
292 identification between apatite and zircon. For phase identification plus high-resolution surface
293 area and volume for 3D grain geometry measurements (as is typical for (U-Th)/He
294 thermochronology), we recommend using a 125 min step scan at 60 kV (2.1 μm resolution).
295 These parameters are optimized for apatite and zircon and can be modified for other minerals of
296 interest. Below, we evaluate the effects of X-ray energy, grain size, and spatial distribution on
297 quantitatively distinguishing zircon from apatite using microCT data.

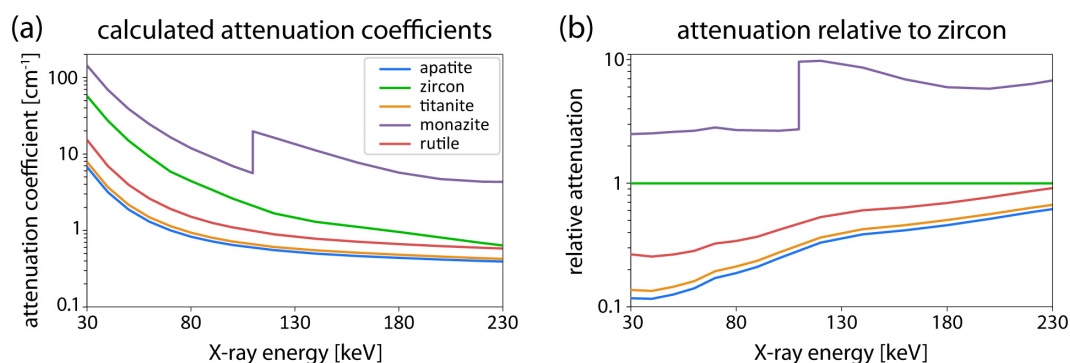
298 **3.1 Theoretical X-ray attenuation**

299 We calculated the theoretical X-ray total attenuation coefficients of apatite, zircon,
300 titanite, monazite, and rutile (Fig. 3a) for a range of X-ray energies commonly used for microCT
301 (~30-230 keV) using MuCalc (<https://www.ctlab.geo.utexas.edu/software/mucalc tool/>), a
302 Microsoft Excel plugin which uses data from the NIST XCOM database of mineral-specific
303 parameters (Hanna and Ketcham, 2017). The modeled attenuation coefficients predict how X-
304 rays interact with different minerals. The greater the difference in attenuation coefficients, the
305 more distinct two mineral phases will appear in microCT data.



306 Based on these calculations, zircon has a much higher attenuation coefficient than apatite
307 across the energy spectrum. At lower energies, the difference between the attenuation
308 coefficients of other minerals relative to zircon (Fig. 3b) is greater than at higher energies. The
309 attenuation coefficients of apatite, zircon, titanite, and rutile converge around 200-300 keV.
310 Thus, energies less than ~200 keV should make zircon grayscale values distinguishable from
311 apatite and other lower attenuation phases (i.e., zircon appears brighter in reconstructed microCT
312 data as seen in Fig. 2). The attenuation coefficients of apatite and titanite are similar at all
313 energies, but display slightly more divergence <80 keV. The observed X-ray attenuation of
314 actual mineral grains might differ from these predictions due to material inhomogeneity,
315 compositional variation (such as endmember mixing and elemental substitution), crystal defects
316 (e.g., metamictization), inclusions, and artifacts due to shadowing from neighboring grains
317 (photon starvation) and beam hardening. In this study, we analyzed our mounts at the maximum
318 achievable voltage on the Rigaku CT Lab HX130 of 130 kV as well as a reduced voltage of 60
319 kV. These parameters may vary for other microCT instruments.

320
321



322
323
324
325
326
327
328

Figure 3: (a) Attenuation coefficients for commonly dated minerals over a range of X-ray energies calculated with MuCalc. (b) The same modeled attenuation coefficient data normalized by zircon. Generally, higher attenuation coefficients mean brighter grayscale values in reconstructed microCT data. A greater difference in attenuation coefficients between mineral phases aids in mineral identification.



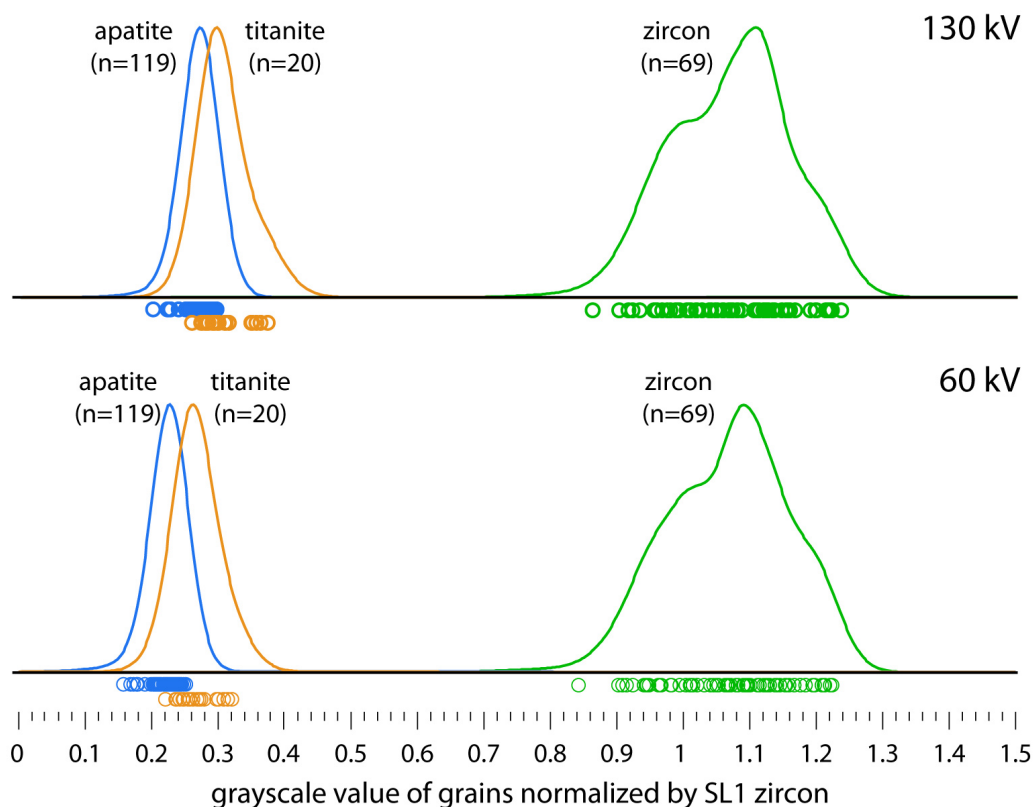
329 **3.2 Normalized grayscale values of grains**

330 We use the 68-minute continuous scans to assess how grayscale values of individual
331 grains (or shards) vary at different scan energies and for different mineral phases. Grayscale
332 values for individual grains of unknowns and standards were normalized by the average value of
333 the SL1 zircon shards on each mount for each set of scan parameters. The absolute grayscale
334 value in the volumes depends on scanning conditions and reconstruction settings, thus internal
335 normalization makes the results comparable and independent of these parameters.

336 We found that apatite grains have grayscale values of about 22% and 27% (at 60 kV and
337 130 kV, respectively) of those of zircon grains (Fig. 4). The distributions are broad due to intra-
338 grain, inter-grain, and inter-sample variability, but the apatite and zircon populations are distinct
339 from each other so that individual grains can be uniquely identified. This also confirms the
340 theoretical modeling (Fig. 3) and the observations of different X-ray attenuation of apatite and
341 zircon grains in the X-ray projections (Fig. 1). The grayscale value distribution of titanite
342 overlaps partially with that of apatite and is sample-dependent, making a phase distinction
343 possible for some but not all grains. For example, the MG1 titanite mineral standard more
344 closely overlaps the apatite grains than the “unknown” titanite crystals picked from USC-FCT1
345 and 2, which are systematically slightly brighter (Fig. 5).

346 The separation between all of the distributions is greater for 60 kV than for 130 kV, as
347 predicted by the theoretical modeling above (Fig. 4). Therefore, volumes from scans at 60 kV
348 can be used to resolve smaller differences in X-ray attenuation than at 130 kV, which does not
349 have a pronounced effect on the apatite-zircon distinction but can be useful when trying to
350 distinguish between apatite and titanite. However, lower energy X-rays are less penetrating and
351 lead to more artifacts and noise in the resulting reconstructed data (Hanna and Ketcham, 2017).
352 Therefore, there is a trade-off between the absolute separation of phases in grayscale-value space
353 and the signal-to-noise ratio, the latter of which can be improved by longer scan times.

354



355

356 Figure 4: Kernel density estimates (KDEs) of all apatite, zircon, and titanite grayscale value
357 measurements (including standards) for 68 min scans calculated with an adaptive bandwidth
358 equal to the standard deviation of grayscale variation within each grain. Each KDE is an
359 aggregation of data from three different sample mounts and shows all individual data points. The
360 grayscale value of each grain was normalized by the average grayscale value of SL1 zircon
361 grains in the same volume. The difference between the attenuation of the three minerals is
362 greater at 60 kV than at 130 kV, as theoretically predicted.

363

364 We observed good reproducibility for average normalized grayscale values of
365 populations of the same sample across the three mounts (Fig. 5). For example, the average
366 normalized grayscale values of Durango apatite shards (UT-DUR) are all within uncertainty at
367 0.255 ± 0.046 (2σ) for Mount A, 0.267 ± 0.016 for Mount B, and 0.272 ± 0.014 for Mount C. Some
368 of these average values are skewed by individual outliers, which are likely due to grain size
369 effects (see Section 3.4).



370 Although average grayscale values across grain populations are reproducible, we observe
371 a range of grayscale values for individual replicate grains from the same sample or of shards
372 from the same crystal (Fig. 5). This may be due to differences in bulk composition and structure.
373 For example, natural apatites are solid solutions of three different endmembers which have
374 different densities. The exact composition of any apatite grain will have an impact on its X-ray
375 absorption and hence the observed grayscale value. Zircon density is mainly controlled by
376 radiation damage (Holland and Gottfried, 1955), which can cause different densities for different
377 grains or of parts of the crystal in the case of pronounced zoning of radioactive elements. The
378 effect of differing grayscale values between different samples is most pronounced between the
379 titanite standard in Mount C and the titanite from FCT samples in Mount B (see Fig. 5). The
380 density of titanite has also been shown to be a function of crystal damage (Vance and Metson,
381 1985).

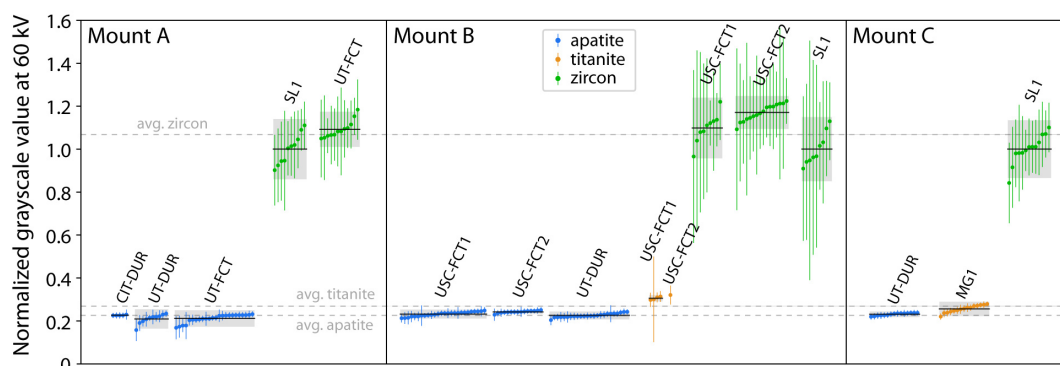
382 We segmented grains based on their outer surface and calculated the average grayscale
383 value of the material enclosed by that surface. It is necessary to exclude the outermost grain
384 boundary because it commonly appears falsely brighter due to beam hardening. However, if
385 there is internal heterogeneity, such as inclusions with higher or lower grayscale values, the
386 observed average grayscale value of any particular grain can be affected (expressed as RSDs).
387 Grains with a large fraction of inclusions of a particular type can therefore change the average
388 grayscale value and might lead to misidentification. One strategy to mitigate this would be to
389 filter certain histographic ranges of values within the segmented grains to exclude inclusions and
390 measure only the average grayscale value of the host grain. Alternatively, this could also be used
391 as a tool to identify individual crystals with inclusions, which would display higher or lower
392 average grayscale values than the rest of the population.

393 The grayscale value distribution within a particular mineral grain is dependent on the
394 natural variation of density and composition (such as zoning) as well as measurement noise. The
395 absolute 2σ -variability of apatite and titanite grains is about 0.01-0.02 for apatite and 0.1-0.2 for
396 60 kV/68 min scans normalized by SL1 zircon (Fig. 5). In relative terms, this is a 5-10%
397 variation for apatite and titanite, and a 10-20% variation for zircon. Measurement noise in the
398 reconstructions is likely not the main contributing factor to this variation in the 68 min scans (see
399 Section 3.4 and Fig. 7). The remaining variations can be due to changes in material parameters
400 across a grain, inclusions of different densities than the host phase, and beam hardening. Overall,



401 the normalized grayscale value can be used to distinguish apatite and zircon, and to some extent
402 other phases such as titanite. Employing strategies to minimize noise and artifacts is important to
403 make this distinction robust for every analyzed mineral grain.

404
405
406



407

408 Figure 5: Mean grayscale values (normalized by SL1 zircon) for all grains measured in 60 kV/68
409 min scans, given with 2σ -variability and organized by mount and sample. Zircon is shown in
410 green, apatite in blue, and titanite in orange, as in the other figures. The average for each sample
411 is given as a black bar with the 2σ -variability shaded in gray. Averages for the whole populations
412 of apatites, zircons, and titanites are given as gray dashed lines. Zircon and apatite populations
413 for all mounts are distinct, while apatite and titanite populations show some overlap. There is
414 observable inter-sample variability in the mean normalized grayscale value of each mineral but
415 values for the same samples (e.g., UT-DUR) are reproducible within error between mounts.

416 3.3 Use of dual-energy data

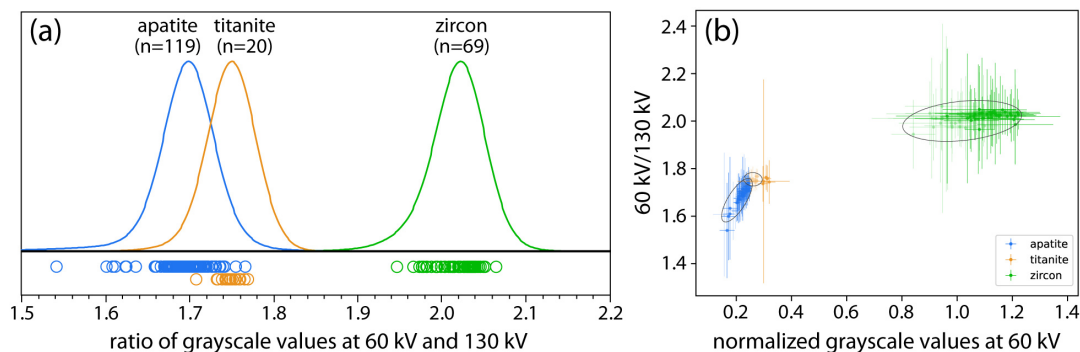
417 The change of the attenuation coefficient with X-ray energy is a function of material
418 density and composition, and is characteristic for each mineral (Alves et al., 2014). Therefore,
419 the ratio of the attenuation at two different X-ray energies can be used as an additional parameter
420 to identify the mineral phase of a grain (e.g. Hanna and Ketcham, 2017). We observed a clear
421 distinction between apatite and zircon in this parameter as well (Fig. 6a). Titanite again appears
422 similar to apatite, but the separation between the two distributions is greater in dual-energy space
423 than in the 60 kV or 130 kV data alone. Therefore, this dual-energy parameter can be used as an



424 additional tool to distinguish phases that have similar absolute attenuation coefficients, and
425 hence appear similar in terms of grayscale values. This necessitates two scans of the same mount
426 at two different energies, as well as additional processing to align the two scans and compute
427 average grayscale values for both scans. However, the resulting data can be used to map regions
428 in dual-energy vs. single-energy plots (Fig. 6b), yielding a more robust phase identification for
429 individual grains.

430

431



432

433 Figure 6: (a) Kernel density estimates of the ratios of the grayscale values at 60 kV and 130 kV
434 for grains from all three mounts. The mounts were scanned at 60 kV and 130 kV with otherwise
435 identical scan parameters and the grayscale values were measured at the same positions. Zircon
436 and apatite form very distinct distributions, and the populations of apatite and titanite overlap but
437 show more separation than grayscale values from scans at a single energy. (b) Dual-energy
438 parameters plotted against normalized grayscale values at 60 kV. Known standards are shown in
439 lighter colors and black lines outline the field of values of standards. Unknown sample grains of
440 apatites and zircons fall almost entirely within the field of standards. Titanite sample grains are a
441 significantly different brightness (grayscale values) than sample grains but have the same dual-
442 energy parameter.

443

444 3.4 Optimizing mount geometry and scan parameters

445 We tested the grayscale variability introduced by grain size, spatial distribution of the
446 grains on a mount, and direction of the mount during microCT data acquisition. Each of these



447 factors can affect the path that X-rays take through the grains and the preferential attenuation of
448 parts of the X-ray spectrum of a polychromatic beam (beam hardening), which can result in
449 artifacts that cause changes of the average grayscale for a given grain unrelated to the actual
450 mineral-specific X-ray attenuation. We found that image quality and signal-to-noise ratio
451 improved with increased scan time (Fig. 7), as is expected based on counting statistics. We
452 quantified variability in our data by calculating the relative standard deviation (RSD) of
453 grayscale value within each segmented grain, which is a measure of both natural variability of
454 the material and any superimposed measurement noise.

455 A clear distinction between apatite and zircon can already be observed in the 18 s scans
456 (Fig. 7), although the RSDs are high (0.2-0.3) for both apatite and zircon grains. The RSDs
457 decline with increasing scan time for otherwise constant experimental conditions (Fig. 6),
458 asymptotically approaching ~ 0.04 for apatite and ~ 0.08 for zircon. The remaining RSDs might
459 reflect the true natural variability of material parameters (density, endmember mixing, crystal
460 damage, elemental substitution, inclusions) within the mineral grains. For the particular
461 instrument and experimental setup employed here, the signal-to-noise ratio did not improve
462 significantly beyond a scan time of 17 min at a reduced resolution (voxel size of $5.7 \mu\text{m}$). For
463 full-resolution reconstructions, a 125 min scan time was sufficient to produce comparable RSDs,
464 while also allowing for a smaller voxel size ($2.1 \mu\text{m}$) which is preferable for obtaining geometric
465 parameters, such as crystal size and shape for FT-corrections (Evans et al., 2008).

466 We also found that the orientation of the mount during data acquisition has a significant
467 effect on the data quality. A vertical orientation, perpendicular to the source and parallel to the
468 detector plane, produced much lower RSDs for the same scan conditions than a horizontal
469 position (Fig. 8). Highly attenuating phases (such as zircon) produce artifacts such as shadowing
470 and streaking (e.g. Hanna and Ketcham, 2017). When these artifacts overlap with other sample
471 grains, they can significantly alter the observed grayscale value of parts of grains which does not
472 reflect their actual X-ray attenuation and leads to erroneous measurements with increased RSDs
473 (Fig. 8). X-rays passing through a horizontal mount traverse several grains in most orientations
474 and produce strongly expressed artifacts, whereas data acquisition in a vertical position
475 significantly decreases the number of rays that pass through more than one grain. Therefore,
476 particularly for samples with highly attenuating phases, we recommend scanning mounts in a
477 vertical position to reduce noise and improve reproducibility. A tilted orientation can achieve



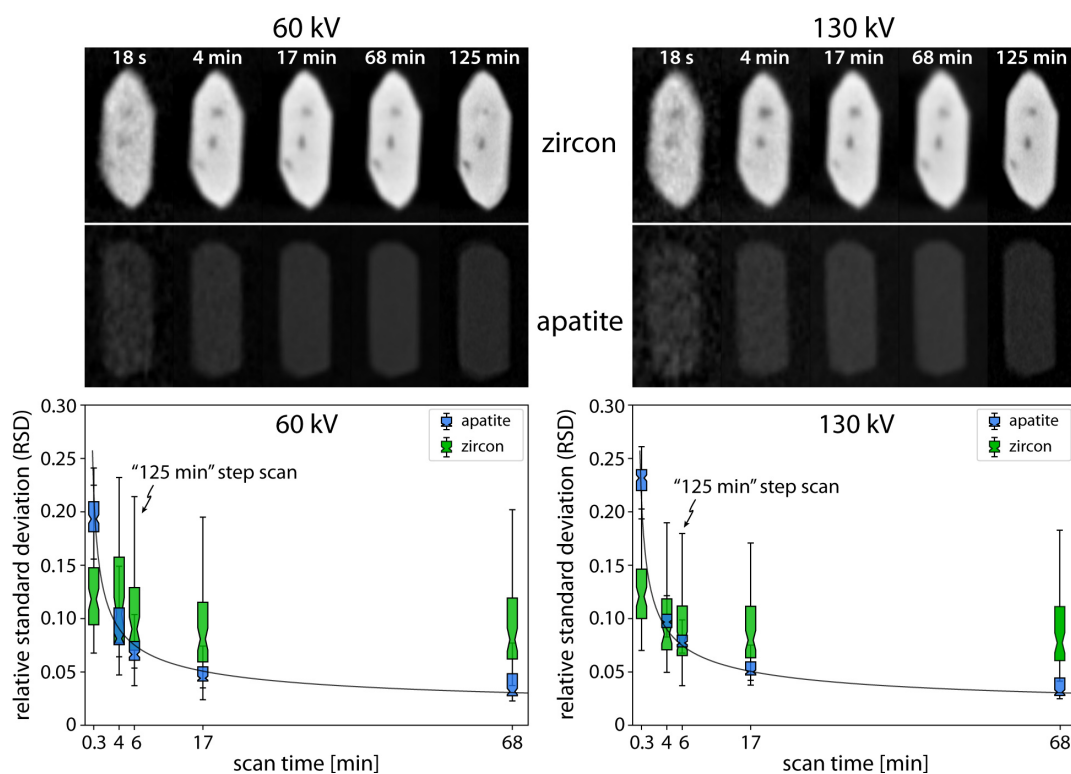
478 similar results but makes data cropping more difficult. Scanning mounts horizontally is another,
479 more common option that may be suitable depending on the phase of interest.

480 The size and arrangement of the grains on the mount also had an influence on the
481 observed grayscale values and their RSDs. We tested these effects with a grain mount (Mount C)
482 composed of only shards of known standards (apatite, zircon, and titanite). For a vertical scan,
483 the horizontal position did not have an observable effect on the measured grayscale values of
484 grains (Fig. 8a) but the vertical position did have a significant effect, with grayscale values
485 decreasing downwards (Fig. 9b). This effect was observed for both apatite and zircon. Titanite
486 showed an even greater dependence on the vertical position, but this trend was exaggerated by
487 the predominance of smaller shards in the top row and larger ones in the bottom row of the
488 mount. These spatial effects are likely caused by the inhomogeneity of the total X-ray
489 attenuation at any height above the sample holder due to clustering of grains at certain heights.
490 These spatial effects can be minimized by distributing known standards throughout the grain
491 mount and normalizing sample grain measurements by the closest standard, and by avoiding
492 lines or grid shapes when placing grains.

493 We observed a general trend of decreasing grayscale values with increasing grain size for
494 the set of all grains of this mount (Fig. 9c). This trend can be explained by beam hardening (see
495 Hanna and Ketcham, 2017), which results from the preferential attenuation of low-energy parts
496 of the X-ray spectrum by highly attenuating material. This effect makes the center of highly
497 attenuating regions appear darker. This artifact can lower the observed average grayscale value
498 of a grain, producing measurements that are not solely related to the attenuation coefficient of a
499 phase. This can be counteracted by choosing standard grains/shards that are matched in size to
500 the unknown sample grains. If beam hardening occurs, it will affect all grains equally, thereby
501 allowing for a direct, unbiased comparison of the average grayscale values of sample grains and
502 standards.

503 The geometric effect discussed above can change the average observed grayscale values
504 of grains by 5-10%. Even with these effects, apatite can still be distinguished from zircon due to
505 their large relative difference in X-ray attenuation. However, precautions should be taken when
506 distinguishing apatite from titanite, which displays a much lower relative contrast (see Figs. 4, 5,
507 6), to ensure that data quality is high and phase identification is robust and unique.

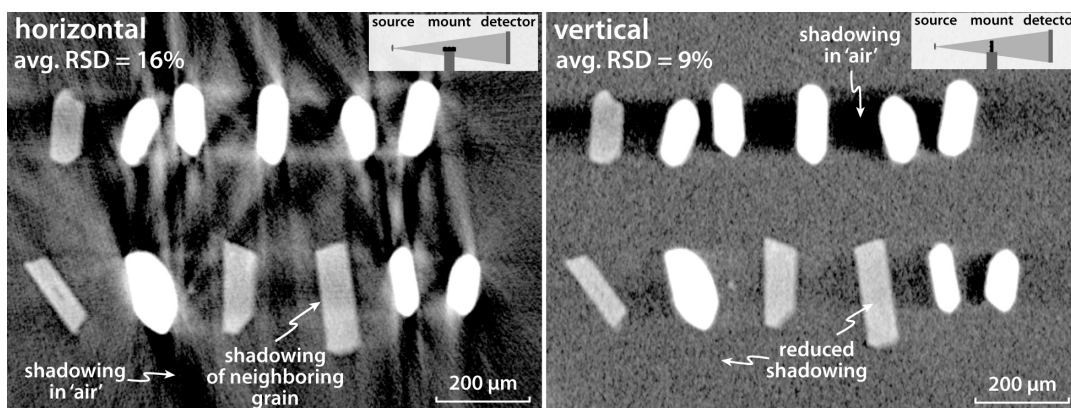
508



509

510 Figure 7: Slices of selected grains (top) and grayscale relative standard deviations (RSDs) of all
511 analyzed apatite and zircon grains (bottom) at different scan times for 60 kV and 130 kV scans.
512 Slices are given at the same contrast settings, showing the difference in grayscale value between
513 apatite and zircon. Scans of 18 s, 4 min, 17 min, and 68 min are processed at a reduced
514 resolution ($5.7 \mu\text{m}$) whereas 125 min scans are processed at full resolution ($2.1 \mu\text{m}$). Image
515 quality and signal-to-noise ratio improve with longer scan times, and graphs of $1/\sqrt{n}$ -functions
516 are given for reference (gray lines). For our instrumental and scan parameters, we did not see
517 significant improvements in signal-to-noise ratio past 17 min.

518

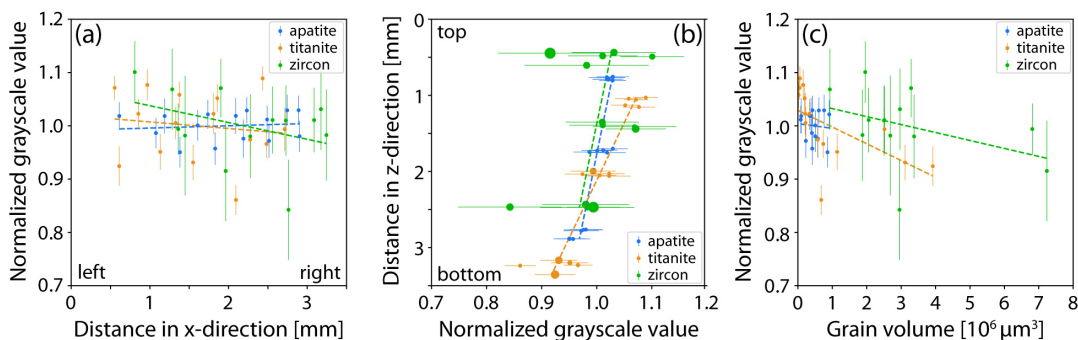


519

520 Figure 8: Slices of horizontal and vertical scans of the same grain mount show the reduction of
521 artifacts for the vertical scan position relative to the horizontal scan position. Highly attenuating
522 zircon (bright) grains produce shadowing artifacts that overlap with apatite (less bright) grains,
523 altering the overall grayscale value measured in the apatite grains. Some shadowing still occurs
524 in the vertical position but is much reduced relative to the horizontal position. This is reflected in
525 the relative standard deviation (RSD) of the grayscale value within each set of grains. The
526 arrangement of grains in a geometric pattern leads to the amplification of artifacts. Note:
527 Photographs have increased contrast to highlight the differences in artifacts.

528

529



530

531 Figure 9: Plots showing the effect of spatial parameters on the grayscale values of the grains on
532 Mount C, which contains shards of known apatite, titanite, and zircon crystals (see Fig. 2). The
533 measured grayscale values have been normalized by the average of all grains of that mineral.
534 Linear regressions (dashed lines) show approximate trends. (a) There is no systematic variation
535 of normalized grayscale values with horizontal distance (x-direction) of grain placement on the



536 mount. (b) The normalized grayscale values of all mineral grains show a dependence on vertical
537 distance (z-direction) on the mount. The trends of decreasing brightness from top to bottom are
538 roughly parallel for apatite and zircon, with around 5% total variation. Titanite shows larger
539 grayscale variations (~10%), which are partly due to variations in the volume of grains (size of
540 symbol correlates with volume). Larger grains are preferentially located at the bottom of the
541 mount, thereby amplifying this trend. (c) Grains of larger volume have lower grayscale values,
542 likely due to the effects of beam hardening.

543 **3.5 Recommended procedures for microCT phase identification for geo- and** 544 **thermochronology**

545 Based on the calibrations above, we have developed a workflow for the identification of
546 apatite and zircon grains in grain mounts for geochronology using microCT. The methodology
547 described here has the potential to eliminate the need for highly toxic heavy liquids (MEI and
548 bromoform), reduce time spent picking grains, and curtail misidentification of apatite and zircon
549 in geo- and thermochronological analyses. Instead, this enables the use of less toxic heavy
550 liquids (LST, LMT, SPT) that produce mixed apatite and zircon separates and users can quickly
551 pick suitable-looking grains without close visual inspection and appraisal of interference colors,
552 crystal shape, etc. If the objective is to simply distinguish between apatite and zircon, then
553 reconstructed grayscale slices of rapidly acquired (~10-20 min) microCT data can be used to
554 visually identify the mineral phase of each grain, requiring little technical training and using
555 freely available software such as ImageJ (Schneider et al., 2012). For a more quantitative record
556 or if the separation of phases with a small, weak density contrast (such as apatite and titanite) is
557 required, grains can be segmented with more specialized software (such as Dragonfly, which
558 offers free academic licenses), and average grayscale values can be extracted for each grain. For
559 many geochronological applications, both apatite and zircon are desirable target phases.
560 Therefore, this method can be used to screen for both minerals at the same time. For the
561 detection of inclusions and the 3-dimensional measurement of grain geometry, this method can
562 be used with microCT scans with longer scan times (~2 h), which can be processed to yield a
563 better spatial resolution.

564 We found that using clear plastic slides (thickness ~0.5 mm) as a base for grain mounts
565 provided the necessary rigid support to hold the grain mounts in place while handling during



566 microCT scanning. These plastic slides have a similar refractive index to glass and can be easily
567 cut with scissors or other implements. Exact mount shapes (circles, squares, rectangles) depend
568 on the scanner set-up. Generally, the goal is to maximize the grain mount surface area to fit a
569 large number of grains on a single mount. As mentioned, double-sided adhesive tape is strong
570 enough to secure mineral grains, even in vertical scans, but different tapes can vary in terms of
571 clarity and glue thickness.

572 Unknown mineral grains can be picked from a separate and placed directly onto the grain
573 mount with tweezers or a needle. The grains should be placed onto the adhesive tape firmly
574 enough to ensure that enough surface area of the grain is in contact with the tape, but not so
575 firmly that the grain breaks. We recommend strategically distributing the unknown grains in such
576 a way that any individual grain can be easily identified after microCT for further analysis. Grains
577 should be spaced at least one grain length apart to minimize the effect of artifacts from highly
578 attenuation phases. Forming lines or a grid of grains should be avoided since these shapes tend to
579 amplify artifacts. Known mineral standards of expected phases should be included on every grain
580 mount. They can be shards of larger crystals or mineral grains that have been identified by an
581 independent method, such as through micro-Raman spectroscopy. These standard grains should
582 broadly match the grain sizes of the unknowns and be distributed throughout the grain mount in
583 the same way as the unknowns to account for any spatial variation in X-ray attenuation. In some
584 cases, the mineral standard can also be used as the age standard for further analysis (e.g.,
585 Durango apatite).

586 Vertical grain mount scans produce overall better results by reducing microCT artifacts
587 (see Fig. 7). However, horizontal scans are likely sufficient in many applications, such as
588 distinguishing apatite and zircon, and allow multiple grain mounts to be stacked on top of the
589 sample holder. This allows 4-times the number of grains in a single scan (up to 400 grains). The
590 resulting file sizes will be bigger, but the scan time is the same.

591 **3.6 Benefits of microCT in geo- and thermochronology**

592 Here we present a rapid method for identifying apatite and/or zircon crystals in separates
593 using microCT as a pre-screening technique. This can serve several purposes depending on the
594 goal of the research. First, it can reduce the misidentification of minerals prior to costly and time-



595 intensive analyses. In the case of precious or low-yield samples, reducing human error is
596 especially important.

597 The 3D grain-specific measurements acquired during the micro-CT scan provide added
598 value to (U-Th)/He thermochronology research where grain shapes are used to calculate Ft
599 corrections and directly impact age calculations. These corrections typically assume a mineral
600 grain geometry and use 2D grain measurements (e.g., Farley et al., 1996). More recent work has
601 used microCT to calculate 3D Ft and/or validate 2D Ft measurements (Evans et al., 2008;
602 Glotzbach et al., 2019; Cooperdock et al., 2019). The method presented here yields data that can
603 be directly used with the Blob3D software for 3D Ft calculation, or provide more precise grain-
604 specific surface area and volume measurements for calculating Ft by hand.

605 For detrital geochronology, the microCT pre-screening method described here can be
606 used to identify mineral phases regardless of grain geometry, thereby enabling the use of grains
607 with less-than-ideal geometries. Since apatite and zircon are mainly picked under a binocular
608 microscope based on their grain shape, sub-euhedral or broken crystals, which typically represent
609 the bulk of the crystals in a given separate, are often not chosen for further analysis. This can
610 present a problem for samples with low yields or bias the results to grains of specific
611 morphologies (i.e., histories or age populations).

612 Furthermore, this method can be expanded beyond apatite, zircon, and titanite. For
613 example, we did not analyze monazite or rutile in this study. However, based on the MuCalc
614 modeling and the characteristics of the microCT scans analyzed here, monazite and rutile should
615 be distinguishable from apatite, zircon, and titanite at X-ray energies below ~200 keV, with a
616 greater distinction between these phases at lower X-ray energies. The separation of common
617 detrital minerals, such as apatite, zircon, titanite, monazite, and rutile in a grain mount, crushate,
618 or rock sample could also be used for detrital heavy mineral analysis.

619 **4 Conclusions**

620 We show that microCT pre-screening of grains picked from separates can be used to
621 unequivocally distinguish apatite and zircon, and to distinguish apatite and zircon from other
622 phases, such as titanite, with a degree of certainty. Normalizing grayscale values of grains from
623 microCT volumes by the average value of a known zircon standard accounted for differences in
624 experimental setup, instrument performance, and processing from one mount to the next. The



625 remaining observed variation of grayscale values within and between grains is likely due to
626 grain-specific natural variability of material parameters, such as crystal damage and elemental
627 substitution.

628 We recommend the following best practices for future studies:

- 629 • Mineral standards for normalization should be matched in size to the unknown samples to
630 account for the effect of beam hardening.
- 631 • Standards should be distributed throughout the mount, and sample grains should be
632 normalized by the closest standard grain to minimize minor spatial effects.
- 633 • The mount should be tilted vertically for the microCT data acquisition to reduce the
634 effect of shadowing from neighboring grains. MicroCT instrument geometries other than
635 the one used here might require different mount orientations.
- 636 • For the particular microCT instrument used here, the signal-to-noise ratio did not
637 improve significantly past 17 min for continuous scans. A step scan of about 2 h (50 min
638 counting time) was sufficient to produce high-resolution data with a usable signal-to-
639 noise ratio.

640 MicroCT scans that are set up according to the recommendations are a robust method to
641 distinguish between apatite and zircon in mounts of selected grains. This offers a possible
642 alternative to separating apatite from zircon using highly-toxic MEI. Grains can be picked
643 directly from separates that have undergone a density separation with non-toxic LST, LMT, or
644 SPT, which is a less laborious and safer process. As an additional benefit, the data acquired in
645 this process can also be used to screen the sample grains for fluid and mineral inclusions and to
646 model alpha-ejection and -implantation corrections for (U-Th)/He dating (Evans et al., 2008;
647 Cooperdock et al., 2019).

648 **Data availability**

649 Reconstructed microCT volumes for all mounts, X-ray energies, and scan times are stored at the
650 USChelium Lab and are available on request.

651 **Author contribution**

652 EHGC and FH conceptualized the study and experimental design with input from AT; AC
653 collected FCT samples; FH, RMC, and AC prepared samples and collected data; all co-authors



654 contributed to data interpretation; FH and RMC prepared figures; EHGC and FH prepared and
655 edited the manuscript draft with input from RMC, AC, AT, and AJC.

656 **Competing interests**

657 AT is a representative for Rigaku Americas Corporation, the company which manufactured the
658 microCT instrument used in this study.

659 **Acknowledgments**

660 We thank Justine Grabiec and Alexia Rojas for help with mineral separation; Danny Stockli and
661 members of the UTChron laboratory for providing Fish Canyon Tuff and Durango samples; and
662 Ken Farley for providing the Caltech Durango sample. We thank Kalin McDannell, Paul
663 O’Sullivan, and Ryan Ickert for useful discussions about heavy liquids safety, and James Metcalf
664 for FCT sampling information. We also thank Alan Gregorski and Aaron Alke for help sampling
665 the FCT.

666

667 **Financial support**

668 This work was supported by Emily H. G. Cooperdock’s University of Southern California start-
669 up funds and a Major Support Funding Grant from the Women in Science and Engineering
670 (WiSE) at the University of Southern California.

671 **References**

- 672 Alves, H., Lima, I., and Lopes, R. T.: Methodology for attainment of density and effective
673 atomic number through dual energy technique using microtomographic images, Appl.
674 Radiat. Isot., 89, 6-12, <https://doi.org/10.1016/j.apradiso.2014.01.018>, 2014.
- 675 Buijs, W., Van Der Gen, A., Mohn, G. R., and Breimer, D. D.: The direct mutagenic activity of
676 α , ω -dihalogenoalkanes in Salmonella typhimurium: Strong correlation between
677 chemical properties and mutagenic activity, Mutat. Res. Lett., 141(1), 11-14,
678 [https://doi.org/10.1016/0165-7992\(84\)90029-0](https://doi.org/10.1016/0165-7992(84)90029-0), 1984.
- 679 Bowring, S. A., and Schmitz, M. D.: High-precision U-Pb zircon geochronology and the



- 680 stratigraphic record, *Rev. Mineral. Geochem.*, 53, 305-326,
681 <https://doi.org/10.2113/0530305>, 2003.
- 682 Cooperdock, E. H., Ketcham, R. A., and Stockli, D. F.: Resolving the effects of 2-D
683 versus 3-D grain measurements on apatite (U–Th)/ He age data and reproducibility,
684 *GChron*, 1, 17-41, <https://doi.org/10.5194/gchron-1-17-2019>, 2019.
- 685 Dragonfly 2021.1 [Computer software]. Object Research Systems (ORS) Inc, Montreal, Canada,
686 2021; <http://www.theobjects.com/dragonfly>.
- 687 Donelick, R. A., O’Sullivan, P. B., and Ketcham, R. A. (2005). Apatite fission-track analysis.
688 *Reviews in Mineralogy and Geochemistry*, 58, 49-94,
689 <https://doi.org/10.2138/rmg.2005.58.3>, 2005.
- 690 Dumitru, T. A., and Stockli, D. F.: A better way to separate apatite from zircon using
691 constriction tubes, *Advances in Fission-Track Geochronology*, 10, 325-330, 1998.
- 692 Evans, N. J., McInnes, B. I., Squelch, A. P., Austin, P. J., McDonald, B. J., and Wu, Q.:
693 Application of X-ray micro-computed tomography in (U–Th)/He thermochronology,
694 *Chem. Geol.*, 257, 101-113, <https://doi.org/10.1016/j.chemgeo.2008.08.021>, 2008.
- 695 Farley, K. A.: (U–Th)/He Dating: Techniques, Calibrations, and Applications, *Reviews in*
696 *Mineralogy and Geochemistry*, 47, 819-844, <https://doi.org/10.2138/rmg.2002.47.18>,
697 2002.
- 698 Farley, K. A., Wolf, R. A., and Silver, L. T.: The effects of long alpha-stopping distances on
699 (U–Th)/He ages, *Geochim. Cosmochim. Acta*, 60(21), 4223-4229,
700 [https://doi.org/10.1016/S0016-7037\(96\)00193-7](https://doi.org/10.1016/S0016-7037(96)00193-7), 1996.
- 701 Farley, K. A., Treffkorn, J., and Hamilton, D.: Isobar-free neon isotope measurements of flux-
702 fused potential reference minerals on a Helix-MC-Plus10K mass spectrometer, *Chem.*
703 *Geol.*, 537, 119487, <https://doi.org/10.1016/j.chemgeo.2020.119487>, 2020.
- 704 Gautheron, C., Pinna-Jamme, R., Derycke, A., Ahadi, F., Sanchez, C., Haurine, F.,
705 Monvoisin, G., Barbosa, D., Delpech, G., Maltese, J., Sarda, P., and Tassan-Got, L.:
706 Analytical protocols and performance for apatite and zircon (U–Th)/ He analysis on
707 quadrupole and magnetic sector mass spectrometer systems between 2007 and 2020,
708 *GChron*, 3, 351-370, <https://doi.org/10.5194/gchron-3-351-2021>, 2021.
- 709 Glotzbach, C., Lang, K. A., Avdievitch, N. N., and Ehlers, T. A.: Increasing the accuracy of (U-
710 Th(-Sm))/He dating with 3D grain modelling, *Chem. Geol.*, 506, 113–125,



- 711 <https://doi.org/10.1016/j.chemgeo.2018.12.032>, 2019.
- 712 Guenther, W. R., Reiners, P. W., and Chowdhury, U.: Isotope dilution analysis of Ca and Zr in
713 apatite and zircon (U-Th)/He chronometry, *Geochem., Geophys., Geosyst.*, 17, 1623-
714 1640, <https://doi.org/10.1002/2016GC006311>, 2016.
- 715 Hauff, P. L., and Airey, J.: The handling, hazards, and maintenance of heavy liquids in the
716 geologic laboratory, USGS Circular 827, <https://doi.org/10.3133/cir827>, 1980.
- 717 Hanna, R. D., and Ketcham, R. A.: X-ray computed tomography of planetary materials: A primer
718 and review of recent studies, *Geochem.*, 77, 547-572,
719 <https://doi.org/10.1016/j.chemer.2017.01.006>, 2017.
- 720 Holland, H. D., & Gottfried, D.: The effect of nuclear radiation on the structure of zircon, *Acta*
721 *Crystallogr.*, 8, 291-300, <https://doi.org/10.1107/S0365110X55000947>, 1955.
- 722 Hughes, J. M., Cameron, M., & Crowley, K. D.: Structural variations in natural F, OH, and Cl
723 apatites, *Am. Mineral.*, 74, 870-876, 1989.
- 724 Ketcham, R. A., and Carlson, W. D.: Acquisition, optimization and interpretation of X-ray
725 computed tomographic imagery: applications to the geosciences, *Comput. Geosci.*, 27,
726 381-400, [https://doi.org/10.1016/S0098-3004\(00\)00116-3](https://doi.org/10.1016/S0098-3004(00)00116-3), 2001.
- 727 Koroznikova, L., Klutke, C., McKnight, S., and Hall, S.: The use of low-toxic heavy suspensions
728 in mineral sands evaluation and zircon fractionation, *J. South. Afr. Inst. Min. Metall.*,
729 108, 25-33, 2008.
- 730 Lafuente, B., Downs, R. T., Yang, H., and Stone, N.: The power of databases: the RRUFF
731 project, in: *Highlights in Mineralogical Crystallography*, edited by: Armbruster, T., and
732 Danisik, R. M., W. De Gruyter, Berlin, Germany, 1-30,
733 <https://doi.org/10.1515/9783110417104-003>, 2015.
- 734 Lippolt, H. J., Leitz, M., Wernicke, R. S., and Hagedorn, B.: (Uranium + thorium)/helium dating
735 of apatite: experience with samples from different geochemical environments, *Chem.*
736 *Geol.*, 112, 179-191, [https://doi.org/10.1016/0009-2541\(94\)90113-9](https://doi.org/10.1016/0009-2541(94)90113-9), 1994.
- 737 McDowell, F. W., McIntosh, W. C., and Farley, K. A.: A precise ^{40}Ar - ^{39}Ar reference age for the
738 Durango apatite (U-Th)/He and fission-track dating standard. *Chem. Geol.*, 214, 249-
739 263, <https://doi.org/10.1016/j.chemgeo.2004.10.002>, 2005.
- 740 Mounteney, I.: The use of lithium heteropolytungstate as an alternative to bromoform for heavy



- 741 media separations, British Geological Survey IR/11/049, Nottingham, UK, 1-20,
742 <http://nora.nerc.ac.uk/id/eprint/519459>, 2011.
- 743 Munsterman, D., and Kerstholt, S.: Sodium polytungstate, a new non-toxic alternative to
744 bromoform in heavy liquid separation, *Review of Palaeobotany and Palynology*, 91, 417-
745 422, [https://doi.org/10.1016/0034-6667\(95\)00093-3](https://doi.org/10.1016/0034-6667(95)00093-3), 1996.
- 746 Osterman-Golkar, S., Hussain, S., Walles, S., Anderstam, B., and Sigvardsson, K.: Chemical
747 reactivity and mutagenicity of some dihalomethanes, *Chem.-Biol. Interact.*, 46, 121-130,
748 [https://doi.org/10.1016/0009-2797\(83\)90011-x](https://doi.org/10.1016/0009-2797(83)90011-x), 1983.
- 749 Roldán-Arjona, T., and Pueyo, C.: Mutagenic and lethal effects of halogenated methanes in the
750 Ara test of *Salmonella typhimurium*: quantitative relationship with chemical reactivity,
751 *Mutagenesis*, 8, 127-131, <https://doi.org/10.1093/mutage/8.2.127>, 1993.
- 752 Schneider, C. A., Rasband, W. S., and Eliceiri, K. W.: NIH Image to ImageJ: 25 years of image
753 analysis, *Nature methods*, 9, 671-675, <https://doi.org/10.1038/nmeth.2089>, 2012.
- 754 Tagami, T., and O'Sullivan, P. B.: Fundamentals of fission-track thermochronology, *Rev.*
755 *Mineral. Geochem.*, 58, 19-47, <https://doi.org/10.2138/rmg.2005.58.2>, 2005.
- 756 Van Bladeren, P. J., Breimer, D. D., Rotteveel-Smijjs, G. M. T., and Mohn, G. R.: Mutagenic
757 activation of dibromomethane and diiodomethane by mammalian microsomes and
758 glutathione S-transferases, *Mutat. Res., Environ. Mutagen. Relat. Subj.*, 74, 341-346,
759 [https://doi.org/10.1016/0165-1161\(80\)90192-2](https://doi.org/10.1016/0165-1161(80)90192-2), 1980.
- 760 Vance, E. R., and Metson, J. B.: Radiation damage in natural titanites, *Phys. Chem. Miner.*, 12,
761 255-260, <https://doi.org/10.1007/BF00310337>, 1985.
- 762 Vermeesch, P., Seward, D., Latkoczy, C., Wipf, M., Günther, D., and Baur, H.: α -Emitting
763 mineral inclusions in apatite, their effect on (U-Th)/He ages, and how to reduce it,
764 *Geochim. Cosmochim. Acta*, 71, 1737-1746, <http://dx.doi.org/10.1016/j.gca.2006.09.020>,
765 2007.
- 766 Weimerskirch, P. J., Burkhart, K. K., Bono, M. J., Finch, A. B., and Montes, J. E.: Methylene
767 iodide poisoning, *Annals of emergency medicine*, 19, 1171-1176,
768 [https://doi.org/10.1016/S0196-0644\(05\)81524-0](https://doi.org/10.1016/S0196-0644(05)81524-0), 1990.
- 769